Applied Surface Science 457 (2018) 891–901

Contents lists available at ScienceDirect

Applied Surface Science

journal homepage: www.elsevier.com/locate/apsusc

Full Length Article

3D heterogeneous wetting microchannel surfaces for boiling heat transfer enhancement

Wei Zhang[a,b], Yongzhi Chai[b], Jinliang Xu[a,b,*], Guanglin Liu[a,b], Yuanzhi Sun[b]

[a] Beijing Key Laboratory of Multiphase Flow and Heat Transfer for Low Grade Energy Utilization, North China Electric Power University, 102206 Beijing, China
[b] Key Laboratory of Condition Monitoring and Control for Power Plant Equipment of Ministry of Education, North China Electric Power University, 102206 Beijing, China

ARTICLE INFO

Keywords:
3D microchannel surface
Heterogeneous wettability
Microstructure
Synergistic effects
Boiling
Bubble dynamics

ABSTRACT

The manipulation of surface wettability, such as the usage of hydrophobic/hydrophilic hybrid surfaces, is a promising method to enhance boiling heat transfer. However, most studies on wettability manipulation are performed on a 2D bare plain surface without considering the influence of microstructures. In order to disclose the synergistic effects of heterogeneous wettability and microstructures, three types of 3D heterogeneous wetting microchannel surfaces (i.e., TS1, TS2, and TS3) that exhibit different wettability combinations of the inner surface and fin top surface are designed, fabricated, and characterized. The inner surfaces of different microchannels exhibit the same porous structures with a contact angle of 113.2° while the fin top surfaces prepared by different technologies exhibit contact angles of 88.6° (TS1), 8.6° (TS2), and 156.1° (TS3). Saturated boiling of water on the surfaces is experimentally investigated. The maximum heat transfer coefficient (HTC) of 365.0 kW/m^2 K is obtained with TS3 and is 6.3 times that of the 2D bare plain surface (BS). The highest critical heat flux (CHF) of 162.7 W/cm^2 is achieved with TS2 and increases by 60% when compared with that of the BS. The synergistic effects of wettability and microstructures on the boiling performance are summarized in terms of two aspects: (1) combinations of microstructures with hydrophobicity contribute to a high HTC at low heat fluxes and small superheat for the onset of boiling since microstructures provide potential bubble nucleation sites and hydrophobicity reduces the energy barrier of the phase change; (2) combinations of microstructures with hydrophilicity lead to a high CHF since microstructures exhibit a strong capillary pumping ability for liquid returning to the heated surfaces and hydrophilicity enhances liquid affinity with respect to the heated surface. Two bubble growth patterns termed ‘oblate bubble growth’ and ‘conical bubble growth’ are identified based on the observations and are observed as closely related to the synergistic effects of wettability and microstructures.

1. Introduction

Boiling is an important process in many industrial applications such as power plants, heat exchangers, and nuclear reactors [1]. Boiling provides an efficient method to transfer high amounts of heat due to the high latent heat of vaporization while maintaining a small temperature increment. A boiling process is divided into several substages including heterogeneous nucleation on a heated surface, bubble growth, coalescence, and subsequent departure from the heated surface [2]. The properties of a heated surface, such as wettability, roughness, and topology, significantly impact boiling performance [3–7]. Thus, surface modification offers an effective method for boiling performance improvement. The key parameters that characterize boiling performance include the wall superheat for the onset of boiling (ΔT_{ONB}), heat transfer coefficient (HTC), critical heat flux (CHF), and wall superheat corresponding to the CHF (ΔT_{CHF}) [8]. The wall superheat denotes the wall temperature increment from the saturation point of water for a given pressure. Based on Hsu’s theory [9], a prerequisite condition for vapor bubble survival and growth in cavity on a heated wall is that the wall and the adjacent liquid layer must be superheated while the extent of the superheat required depends on the surface properties such as wettability, roughness, and structure. With respect to the application of a given heat flux on a heated surface, a decrease in the wall superheat indicates improvements in the boiling heat transfer performance. As shown in Fig. 1, an enhanced boiling surface is expected to exhibit a lower ΔT_{ONB}, higher HTC, and higher CHF with a lower when compared with those in the original base surface, and the boiling curve for the enhanced surface shifts towards the left.

Currently, two main strategies of surface modification are used for boiling heat transfer enhancement. The aim of the first strategy involves

* Corresponding author at: Beijing Key Laboratory of Multiphase Flow and Heat Transfer for Low Grade Energy Utilization, North China Electric Power University, 102206 Beijing, China.
E-mail address: xjl@ncepu.edu.cn (J. Xu).

https://doi.org/10.1016/j.apsusc.2018.07.021
Received 6 March 2018; Received in revised form 2 July 2018; Accepted 3 July 2018
Available online 04 July 2018
0169-4332/

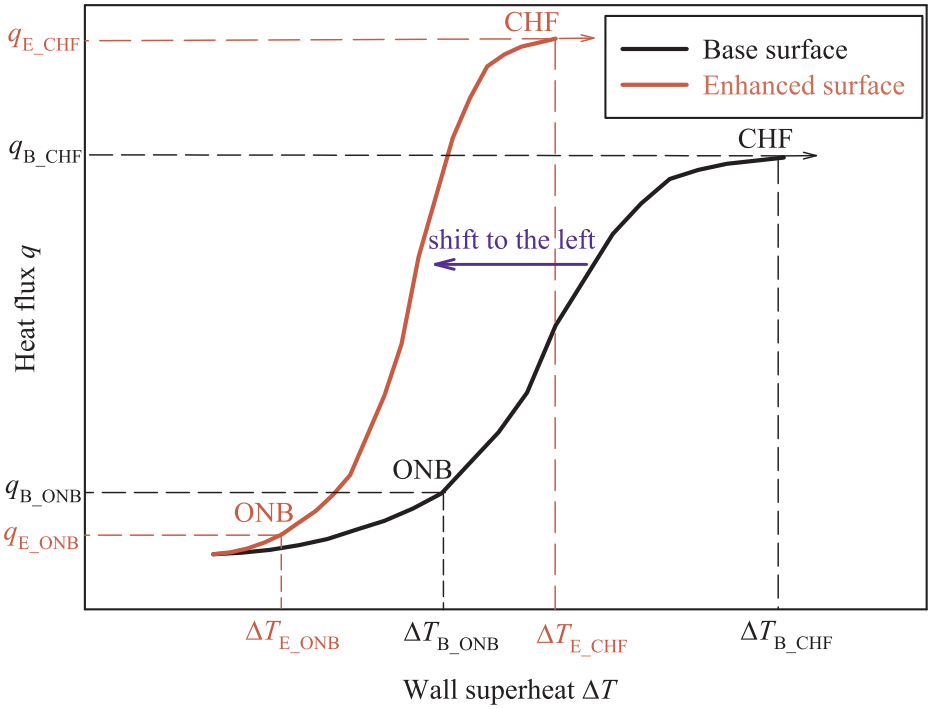

Fig. 1. Schematic of the boiling curves.

improving the boiling performance at low heat fluxes, and this is achieved by promoting bubble nucleation and thereby enhancing HTC. The technologies for the first strategy include reducing the surface wettability [10,11], roughening the surface [12], etching artificial cavities [13], and coating micro/nano structures [14–17]. The second strategy involves increasing the tolerance limit for extremely high heat fluxes, i.e., enhancing the CHF. The technologies for the strategy include increasing surface wettability [18,19] to obtain a higher liquid affinity and using capillary wicking structures [20] to promote liquid rewetting.

Surface wettability manipulation provides a flexible method for boiling heat transfer enhancement. For example, a reduction in wettability easily triggers bubble nucleation due to the decrease in the energy barrier of liquid/vapor phase change [21,22]. The increase in the bubble nucleation density and bubble generation frequency lead to a high dissipation rate of latent heat and increase HTC. Conversely, a hydrophilic surface exhibits a better liquid affinity ability, and this postpones the initiation of dry-out. The increased wettability facilitates the liquid rewetting of heated surface, and thereby increases CHF [18]. However, a homogeneous wetting surface is either hydrophilic or hydrophobic and does not satisfy multiple demands at different stages of boiling. For example, the CHF occurs earlier for a hydrophobic surface since several bubbles tend to adhere to the surface and aggregate into a large vapor film at high heat fluxes, blanket the heated surface, and hinder the liquid rewetting to the heated surface. Conversely, for a hydrophilic surface, ΔT_{ONB} increases and HTC decreases due to the lack of active bubble nucleation sites. In comparison, the heterogeneous wetting surfaces that juxtapose hydrophilic and hydrophobic areas, are observed as a promising technique to equipoise the multiple goals of boiling performance improvement including a lower ΔT_{ONB}, higher HTC, and higher CHF. For example, Betz et al. [23,24] investigated boiling heat transfer characteristics on surfaces with mixed hydrophilic and hydrophobic areas and observed that surfaces with networks combining hydrophilic and hydrophobic regions significantly enhanced CHF and HTC during pool boiling by 65% and 100%, respectively, when compared to those of a plain hydrophilic surface. Jo et al. [25] investigated the nucleate boiling on several heterogeneous wetting surfaces and the ratio of the region covered by hydrophobic dots and observed that the diameter of hydrophobic dots and pitch distance exhibit different effects on the boiling performance. He et al. [26] observed that an enhanced mixed-wettability evaporator surface enhances the heat transfer performance of a two-phase loop thermosiphon. Hsu et al. [27] investigated horizontal copper cylinder surfaces with two mixed types of wettability in pool boiling heat transfer and concluded that the area ratio and spatial configuration of the mixed surface influenced boiling heat transfer and bubble dynamics. Sujith et al. [28] fabricated three different heterogeneous wetting copper surfaces using a screen printing technique and investigated the effect of the wettability gradient on bubble dynamics. A leftward shift in pool boiling curves was observed with the heterogeneous wetting surface. The maximum HTC increased by 95% when compared with that of the plain reference.

The aforementioned studies demonstrate the superiority of heterogeneous wetting surface to homogeneous wetting surface with respect to enhancements in the boiling performance. However, most investigations are conducted in 2D bare plain surfaces and focus on the effects of wettability while neglecting the influences of microstructures. Recently, Jo et al. [29] performed a pioneer study on 3D heterogeneous wetting surfaces for boiling heat transfer enhancement. They observed that the micro-pillars in heterogeneous wetting surfaces interrupted bubble expansions and coalescences, delayed the formation of the large vapor mushroom, and thereby enhanced the CHF. However, there is a paucity of studies that focus on the effects of 3D heterogeneous wetting surfaces on boiling, and there is a significant lack of knowledge on the synergistic effects of wettability and microstructures. The objective of the study involves investigating the boiling heat transfer characteristics on 3D heterogeneous wetting surfaces with different wettability combinations and further revealing the synergistic effects of wettability and microstructures on boiling heat transfer performance. The main contributions of the study include: (1) designing and fabricating three types of 3D heterogeneous wetting microchannel surfaces; (2) evaluating pool boiling performance of water on the surfaces; (3) revealing the heat transfer mechanism and synergistic effects of wettability and microstructure; and (4) visualizing bubble dynamics and identifying bubble patterns in different surfaces.

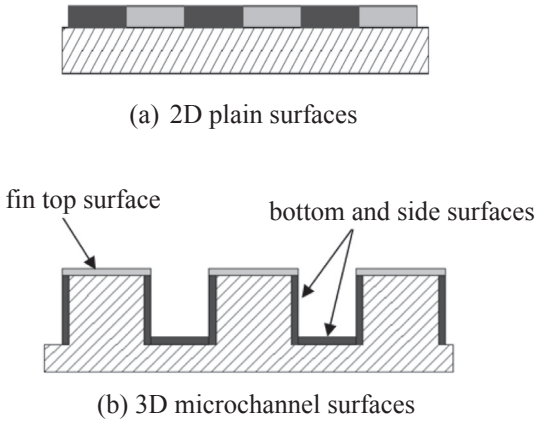

Fig. 2. Concept of 3D hydrophilic/hydrophobic hybrid surfaces. (The black and grey indicate different wetting properties.)

2. Surface design, fabrication, and characterization

The conceptional design of the 3D heterogeneous wetting microchannel surface is shown in Fig. 2. Fig. 2a shows the ordinary 2D heterogeneous wetting surface where the hydrophilic and hydrophobic regions are juxtaposed without an altitude difference, and the structure is similar to those developed by Betz et al. [23], Jo et al. [25], and He et al. [26]. The 3D heterogeneous wetting microchannel surface proposed in the present study is shown in Fig. 2b and is composed of three sub-surfaces including the sidewall of the channel, bottom surface of the channel, and top surface of the fin. The entire inner surfaces of the microchannel including the sidewall and bottom surface exhibit the same wetting properties while the fin top surface exhibits a different wetting property. Based on the conceptional design, three types of 3D heterogeneous wetting microchannel surfaces that exhibit different combinations of the wetting property for the inner wall and fin top surface are fabricated using electrical discharge machining (EDM) and surface modification technologies (Fig. 3). The fabrication for all three type test surfaces (TS1, TS2, and TS3) commences from a bare copper surface polished with a 5000-grit sandpaper (BS). Specifically, TS1 is directly manufactured on BS by EDM in which the fin top surface retains the original status of BS. With respect to TS2, thermal oxidation of BS is first conducted at 400 °C to form an oxidized copper layer, and EDM is subsequently used to fabricate the microchannel. In a manner different from TS1, the fin top surface of TS2 corresponds to a thermally oxidized copper surface (TOS). With respect to TS3, the first step also involves the thermal oxidation of BS to form TOS, and TOS is subsequently immersed in a fluorosilane/ethanol solution with a concentration of 1% (w/w) for 1 h, and EDM is subsequently used to manufacture the microchannel. The fin top surface of TS3 corresponds to a fluoridized copper oxide surface (FOS). It is noted that all the inner surfaces of the microchannel correspond to EDM fabricated copper surface (EDMS) for TS1, TS2, and TS3, which exhibit identical wetting property and surface topologies.

Table 1
Contact angles of water droplets on different surfaces.

BS	EDMS	TOS	FOS
			
88.6°	113.2°	8.6°	156.1°

The contact angles of 3.5 μL deionized water droplet on different surfaces are measured using a contact angle tester (Dataphysics OCA15plus, Germany) with an accuracy of ± 0.1°. Given the difficulties in the direct measurement of the contact angles for the channel inner surface and fin top surface, four sample plain surfaces are prepared with the same fabrication technologies as those used in the 3D heterogeneous wetting surfaces. As shown in Table 1, the contact angles for the BS, EDMS, TOS, and FOS are 88.6°, 113.2°, 8.6°, and 156.1°, respectively. Thus, the BS is slightly hydrophilic (nearly neutral), EDMS is hydrophobic, TOS is almost superhydrophilic, and FOS is superhydrophobic. The combinations of EDMS (microchannel inner surface) with BS, TOS, and FOS (three types of fin top surfaces) constitute the 3D heterogeneous wetting surfaces of TS1, TS2, and TS3, respectively.

The topologies of different surfaces are characterized by SEM (HITACHI, SU-8010, Japan). Fig. 4a shows the morphology of the bare copper surface polished by a 5000-grit sandpaper where sparse cavities with the size of hundred nanometers to several micrometers are randomly distributed. With respect to the EDM fabricated copper surface shown in Fig. 4b, irregular porous microstructures with multiscale pores and cavities are produced via electric spark discharging. Fig. 4c shows the surface morphology of the thermally oxidized copper surface where oxidized copper particle stacks and clusters of 100–500 nm are formed. Additionally, as shown in the upper right illustration in Fig. 4c, irregular gulfs exist among the particle stacks and particle clusters.

3. Boiling experiments

3.1. The test section and experimental setup

Four test surfaces including BS, TS1, TS2, and TS3 were directly fabricated on the top surface of a copper block, respectively. As shown in Fig. 5a, all the four test surfaces correspond to 15 mm × 15 mm square areas. With respect to the 3D microchannel surfaces (TS1, TS2, and TS3), the cross section of the microchannel is rectangular with a depth of 0.8 mm and width of 0.6 mm (Fig. 5b). Near the bottom

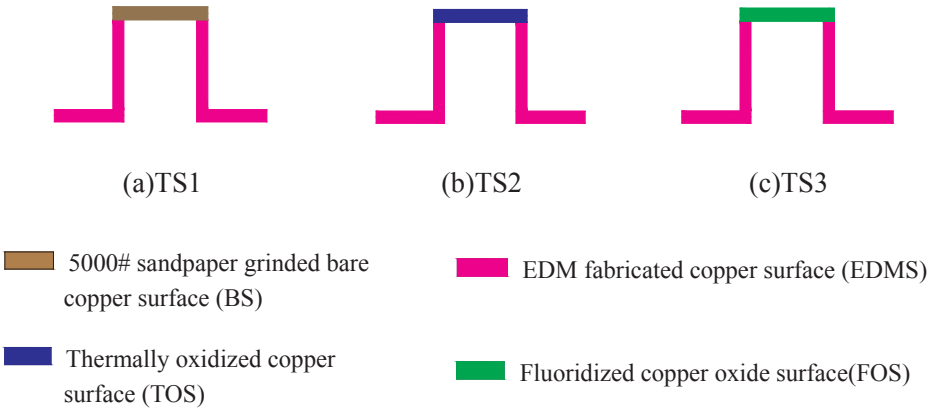

Fig. 3. Three types of 3D heterogeneous wetting microchannel surfaces.

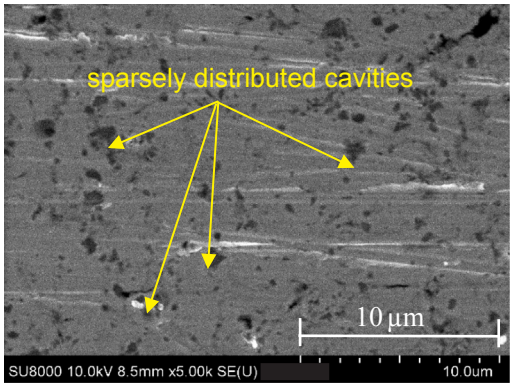

(a) Bare copper surface

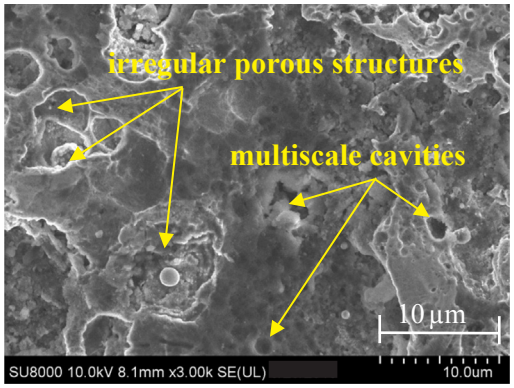

(b) EDM fabricated copper surface

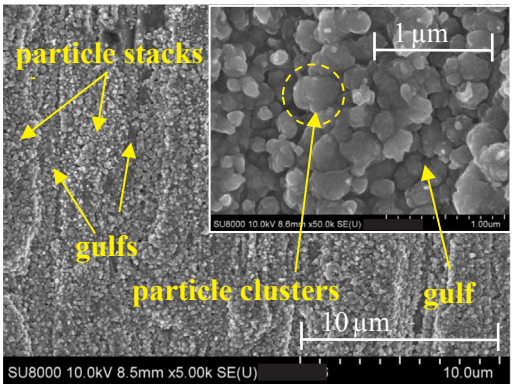

(c) Thermally oxidized copper surface

Fig. 4. Surface topologies obtained with different fabrication methods.

surface of the copper block, five cartridge heaters were inserted inside the copper block to provide the heat flux for boiling (Fig. 5a). Three K-type thermocouples with an equal spacing of 5.0 mm were arranged to measure the temperature distribution along the heat flow direction (Fig. 5b).

Fig. 6 shows a schematic of the pool boiling experimental setup used in the present study. The main components consist of a copper block, a water pool, a power supply module, a condenser, an auxiliary heater, a high-speed camera, and a data acquisition system. The test surface fabricated on the top of the copper block is immersed in water. The water pool is 200 mm wide, 200 mm long, and 400 mm high, and its side wall consists of Pyrex glass that facilitates the visualization of bubble dynamics. The liquid level inside the pool is 300 mm. In order to maintain the mass conservation inside the pool, a coiled condenser was

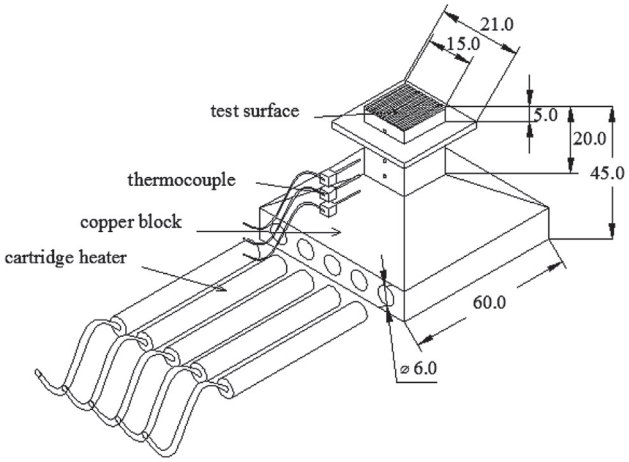

(a) Schematic of the test section assembly

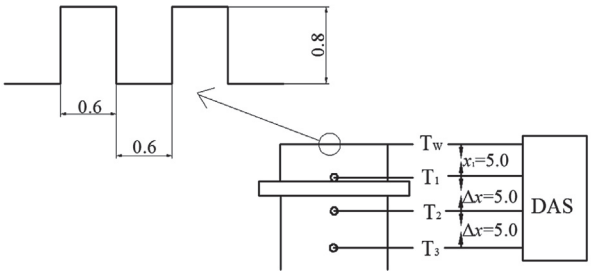

(b) Microchannel dimensions and thermocouple arrangement

Fig. 5. Test section (unit: mm).

placed on the top inside the pool. The auxiliary electric heater was used to maintain the pool temperature at the saturated state of atmosphere pressure. The copper block outside the pool was wrapped with thermal insulation material to reduce heat loss. A high-speed camera (XIMEA, XIQ, Germany) was used to record the bubble behavior. A PXIe-1073 data acquisition system with PXIe-4353 temperature module (National Instruments, USA) was used to record the temperature. A LabVIEW (National Instruments, USA) virtual instrument program was used to display and calculate the surface temperature and heat flux.

3.2. Data reduction and uncertainties

The heat flux to the test surface is calculated based on one-dimensional Fourier heat conduction equation as follows:

$$q = -K_{Cu}\frac{dT}{dx} \tag{1}$$

where K_{Cu} denotes the thermal conductivity of copper, and dT/dx denotes the temperature gradient along the heat flow, which is calculated using the three-point backward Taylor's series approximation as follows:

$$\frac{dT}{dx} = \frac{3T_1 - 4T_2 + T_3}{2\Delta x} \tag{2}$$

where T_1, T_2, and T_3 denote the temperatures along the heat flow as shown in Fig. 5b, and Δx denotes the distance between the adjacent thermocouples. The test surface temperature T_w is derived as follows:

$$T_w = T_1 - q\left(\frac{x_1}{k_{Cu}}\right) \tag{3}$$

where T_1 denotes the boiling surface temperature. Additionally, x_1 denotes the distance between the boiling surface and thermocouple T_1; and

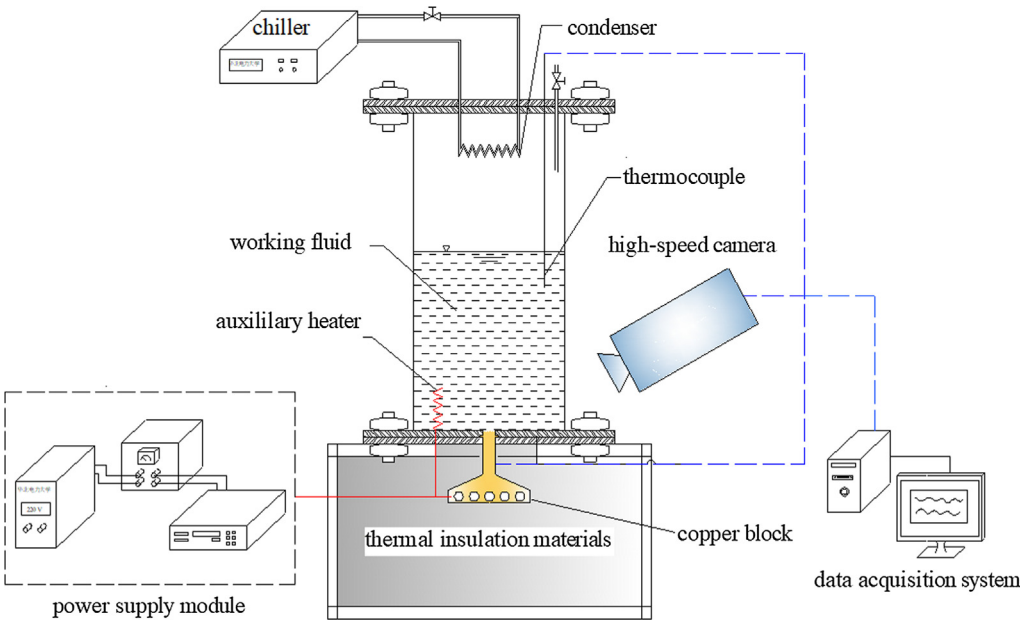

Fig. 6. Pool boiling experimental setup.

x_1 is equal to 5.0 mm for all the test surfaces.

The boiling HTCs are determined as follows:

$$h = \frac{q}{T_w - T_{sat}} \tag{4}$$

where T_{sat} denotes the saturated temperature of water inside the pool.

The accuracy of the K-type thermocouples used in the present study is ± 0.2 °C. The thermal efficiency of the experimental setup is measured to exceed 90% in the present data range. The uncertainty of heat flux is determined by error transfer analysis [30] performed by Jaikumar et al. [14] and Ji et al. [31] as follows:

$$\frac{\Delta q}{q} = \sqrt{\left[\left(\frac{\Delta k_{Cu}}{k_{Cu}}\right)^2 + \left(\frac{3\Delta T_1 \cdot k_{Cu}}{x \cdot q}\right)^2 + \left(\frac{4\Delta T_2 \cdot k_{Cu}}{x \cdot q}\right)^2 + \left(\frac{\Delta T_3 \cdot k_{Cu}}{x \cdot q}\right)^2 + \left(\frac{\Delta x}{x}\right)^2\right]} \tag{5}$$

Fig. 7 shows the variation in the uncertainty with respect to the heat flux. The value of uncertainty decreases sharply with increases in the heat flux. At low heat fluxes, the highest uncertainty is approximately 20% while the uncertainty is lower than 3% when the heat flux approaches the CHF. Prior to the boiling experiments, the water in the pool was boiled for at least 1 h to dissipate any incondensable gases. During the experimental procedures, the auxiliary heater that is connected with an electronic thermostat is used to control the bulk temperature of the pool. The power to the cartridge heater is increased in steps when the bulk liquid attains the saturation temperature. When the thermocouple fluctuations do not exceed ± 0.2 °C in a duration of 10 min, the temperatures are recorded by the data acquisition system. It is noted that all the tests in the present study are performed in atmospheric pressure conditions.

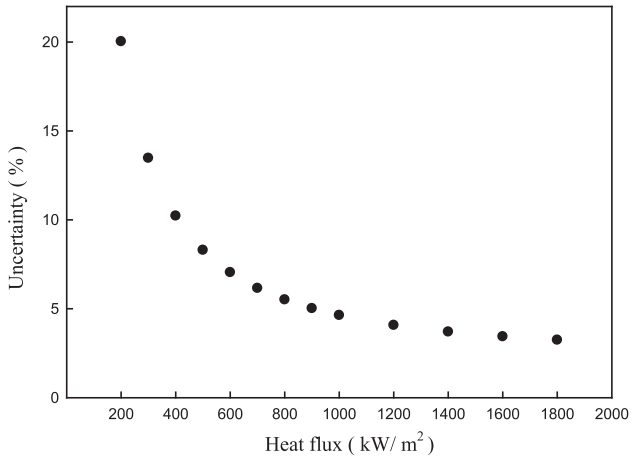

Fig. 7. Variations in uncertainty with respect to the heat flux.

4. Results and discussion

4.1. Boiling curves and HTCs

Four different surfaces, namely BS, TS1, TS2, and TS3 are tested in the present experiments, where BS serves as the baseline for comparisons of boiling enhancement performance. The experiments commenced from a low heat flux prior to the ONB point and stopped until the heat flux reached the CHF, and this is indicated by a sudden temperature rise. Fig. 8 shows the boiling curves and HTCs for all the four test surfaces. As shown in Fig. 1, the boiling curves of all the 3D heterogeneous wetting microchannel surfaces (TS1, TS2, and TS3) shifted to the left when compared to that of the BS (Fig. 8a), thereby indicating that the boiling heat transfer enhancement is obtained when compared to that of the bare surface. The wall superheat of BS maintained a moderate increase with increases in the heat flux. However, the profiles of boiling curve for the 3D microchannel surfaces are completely different. When the heat flux is low, the wall superheat slightly increases with increases in the heat flux. This is because the boiling in the region is not fully developed. With continuous increase in the heat flux, the wall superheat is sufficiently high to activate as many bubble nucleation sites as possible for fully developed boiling. When the boiling is fully developed, the wall superheat does not exhibit a significant change with increases in the heat flux, and this indicates that the applied heat is effectively dissipated by the boiling heat transfer with only a small temperature increment, thereby leading to a high HTC. As shown in Fig. 8b, the HTCs for all the four surfaces increase with increases in the heat flux. The 3D heterogeneous wetting microchannel surface (TS1, TS2, and TS3) significantly enhanced HTC. Specifically, the TS3 that exhibits hydrophobic inner surfaces and superhydrophilic

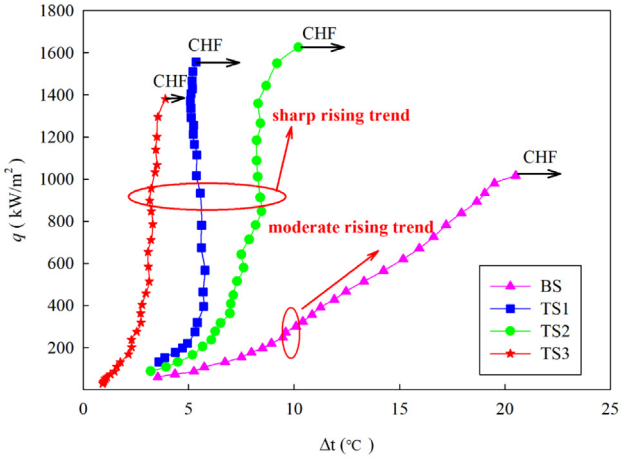

(a) Boiling curves

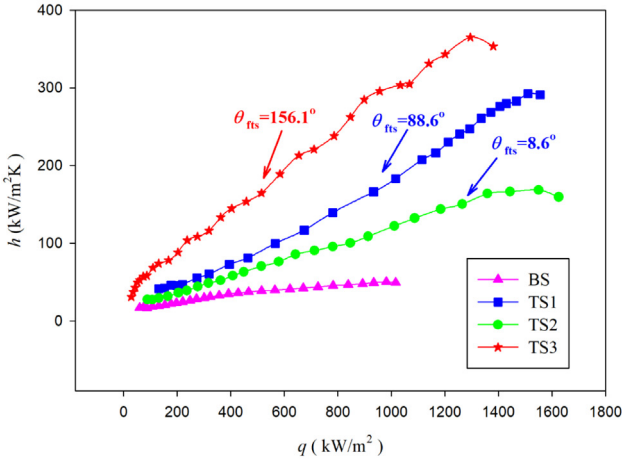

(b) Heat transfer coefficient vs. heat flux

Fig. 8. Boiling curve and heat transfer coefficients for different surfaces.

fin top surface exhibits the maximum HTC for certain heat fluxes in most cases. Additionally, with respect to the 3D microchannel surfaces with the same hydrophobic inner surface, HTC is inversely proportional to wettability, and thus an improvement in the wetting fin top surface (smaller contact angle on fin top surface, θ_{fts}) leads to a decrease in the HTC.

4.2. Quantitative boiling performance comparisons

Four key parameters including ΔT_{ONB}, HTC_{max}, CHF, and ΔT_{CHF} are used for the quantitative comparisons of boiling performance. Specifically, ΔT_{ONB} is a crucial parameter for electronic cooling since a delayed ONB could cause thermal shocks, which are specifically detrimental to the long-term system stability [32]. Fig. 9a shows the ONB for different surfaces. The results indicated that TS3 and BS exhibits the minimum and maximum ΔT_{ONB} corresponding to 1.0 °C and 9.6 °C, respectively, while TS1 and TS2 exhibits close ΔT_{ONB} values corresponding to 3.2 °C and 3.5 °C, respectively. Thus, when compared with the BS, the 3D heterogeneous microchannel surfaces of TS1, TS2, and TS3 reduced the ΔT_{ONB} by 6.4 °C, 6.1 °C, and 8.6 °C, respectively. The ONB is influenced by several factors such as cavity size, surface roughness, surface wettability, and surface morphology. The decrease in the ΔT_{ONB} of TS1, TS2 and TS3 than BS is explained in terms of two aspects. First, the inner surfaces of the 3D microchannel surface (EDMS) exhibits irregular porous microstructures with a wide size range of pores and cavities (Fig. 4b), and it is easy to activate bubble nucleation under a low superheat due to the gases trapped in the pores and cavities

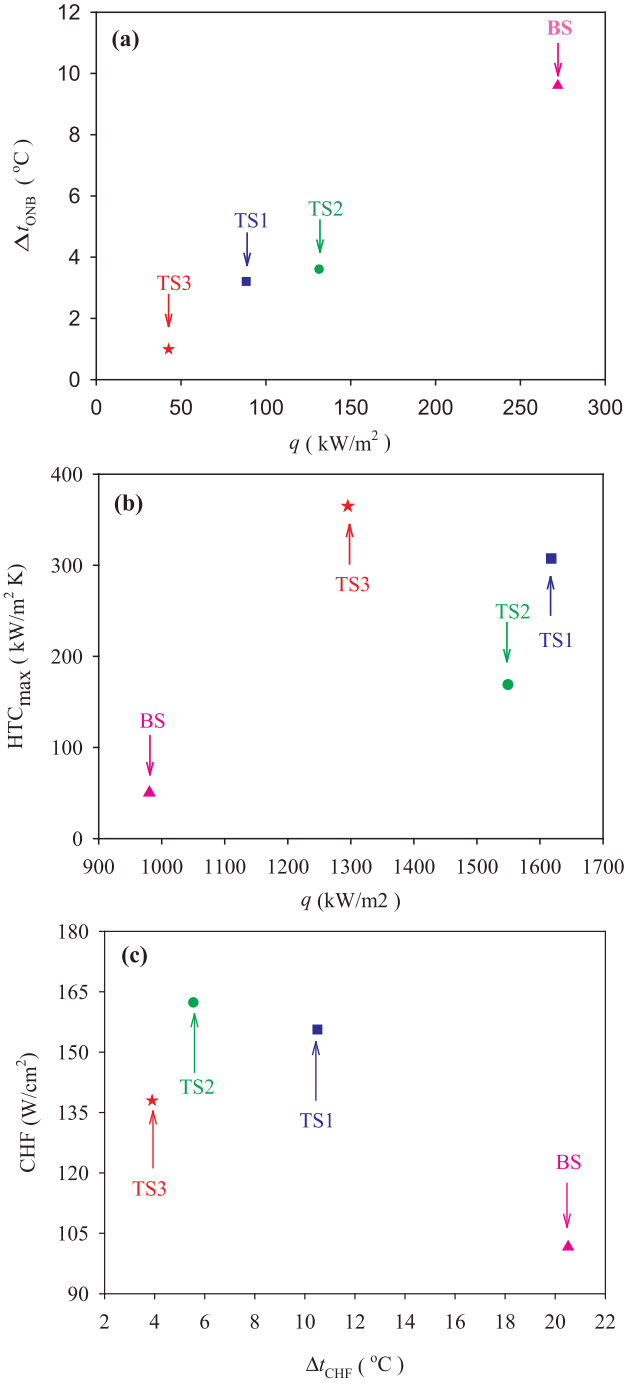

Fig. 9. Comparison of heat transfer performance. (a) superheat vs. heat flux for the onset of boiling; (b) the maximum heat transfer coefficient vs. heat flux; (c) the critical heat flux vs. superheat.

[33]. Second, EDMS is hydrophobic and exhibits a lower interfacial energy barrier for liquid/vapor phase change when compared with that of the hydrophilic BS [21]. In addition to the microstructured hydrophobic inner surface, TS3 exhibits a nanostructured superhydrophobic fin top surface. The synergistic effects of micro/nano structures and superhydrophobicity are responsible for the lowest ΔT_{ONB} of TS3.

Fig. 9b shows the maximum HTC on different surfaces where TS3 exhibits the maximum HTC of 365.0 kW/m^2 K, which is 6.3 times that of BS (50.3 kW/m^2 K). Based on the classic microconvection model of Mikic and Rohsenow [34], the HTC of the heterogeneous wetting surface is described as follows:

$$\mathrm{HTC} = 2(\pi k_l \rho_l c_{pl})^{0.5}[(f^{0.5} d^2 n_a)_{\text{inner surface}} + (f^{0.5} d^2 n_a)_{\text{fin top surface}}] \quad (6)$$

where k_l, ρ_l, and c_{pl} denote the conductivity, density, and heat capacity, respectively, of the liquid phase, f denotes the frequency of bubble departure, d denotes the diameter of bubble departure, n_a denotes the density of active nucleation site. When compared to the BS with randomly distributed sparse cavities (Fig. 4a), TS1, TS2, and TS3 exhibit numerous pores or cavities with sizes ranging from hundreds of nanometers to several micrometers, and this can potentially contribute to the higher HTC. The influence of wettability on the active nucleation sites is described as follows [35]:

$$\frac{r_{\min}}{r_{\max}} = \frac{\delta_t K_1}{2K_2}\left[1 \mp \sqrt{1 - \frac{8K_2\sigma T_{\text{sat}}}{\rho_v h_{\text{fg}} \delta_t \Delta T_w}}\right] \quad (7)$$

where δ_t denotes the thickness of thermal boundary layer, σ denotes the interfacial tension, T_{sat} denotes the saturated temperature, denotes the vapor density, h_{fg} denotes the latent heat of vaporization, ΔT_w denotes the wall superheat, K_1 and K_1 are constants determined by wetting property, and $K_1 = \sin\theta$, $K_2 = 1 + \cos\theta$. As shown in Eq. (7), the size range of activated nucleation sites increases with increases in the contact angles. Given that TS1, TS2, and TS3 exhibit the same inner surface, the difference in HTC is assumed as caused by the differences in the fin top surface based on Eq. (6). Based on Eq. (7), a more hydrophobic top surface with a higher contact angle leads to a higher HTC, and this explains as to why TS3 exhibits the maximum HTC.

Fig. 9c shows the CHF values of BS, TS1, TS2, and TS3 that correspond to 101.6 W/cm^2, 155.6 W/cm^2, 162.7 W/cm^2, and 138.9 W/cm^2, respectively. The CHF occurs in the case that bubbles are sufficiently large to merge and form a continuous vapor film between the liquid and the heated surface, thereby preventing the liquid rewetting and leading to a sharp increase in the wall superheat. Given the strong nonlinear nature of the thermofluidic transport processes occurring near the heated surface, it is extremely difficult to establish a consensus physical model. A widely-used CHF model of boiling on a plain surface was developed by Zuber [36] and was based on Helmholtz instability that merges individual bubble columns. The typical pitch (corresponding to the critical instability wavelength) λ between the bubble columns is determined by the Taylor instability as follows:

$$\lambda_p = 2\pi\sqrt{\frac{3\sigma}{g(\rho_l - \rho_v)}} \quad (8)$$

where σ denotes the interfacial tension, and ρ_l and ρ_v denote liquid and vapor densities, respectively. In the present study, the CHF value of BS is 101.6 W/cm^2, and this is close to the predicted CHF value of 110 W/m^2 as given by Zuber's model. The CHF enhancement in TS1, TS2, and TS3 is interpreted in terms of two mechanisms. First, the porous and mciro/nano structures of TS1, TS2, and TS3 provide several active nucleation sites, and the random distance of cavities changes the instability wavelength. Hence, Zuber's model is extended to a surface with pores and microstructures, and the enhanced CHF is obtained as follows [37]:

$$q_{\text{CHF\_en}} = q_{\text{CHF\_P}}\left(\frac{\lambda_p}{\lambda_\mu}\right)^{0.5} \quad (9)$$

where $q_{\text{CHF\_P}}$ denotes the CHF of plain surface, and λ_p and λ_μ denote the critical instability wavelengths. It is not easy to determine the practical λ_μ with the current surface structures and the $q_{\text{CHF\_en}}$ is 738 W/cm^2 assuming that λ_μ corresponds to the pitch of microchannels (600 μm). However, the maximum CHF obtained with TS2 is 162.7 W/cm^2, and this indicates that other limiting factor can limit the increase in CHF. Second, another mechanism for CHF is attributed to the capillary wicking limit. A surface with a high capillary pumping force brings liquid back to the heated surface, and this prevents the occurrence of dry-out and delays the onset of CHF [38]. Furthermore, a hydrophilic surface exhibits better affinity with liquid than a hydrophobic surface, thereby leading to the CHF enhancement. In the present study, the TS2 exhibits nanostructured hydrophilic surfaces in which the synergistic effects of nanostructures and hydrophilicity lead to a high capillary pumping force and good liquid affinity, thereby enhancing the liquid rewetting and delaying the occurrence of dry-out. Furthermore, the CHF is also affected by the balance between liquid rewetting and vapor escaping. Based on the investigations by Ji et al. [31], a well-designed porous surface for boiling should be multiscale with small pores enhancing the capillary liquid pumping effect and large pore facilitating the escape of vapor. With respect to the fin top surface of TS2, as shown in Fig. 4c, the hydrophilic nanostructured particle stacks and particle clusters provide high capillary liquid pumping force while the gulfs among the tacks and clusters facilitate the escape of vapor. Jo et al. [29] investigated boiling characteristics with controlled wetting patterns and micro-posts. It is observed that the micro-posts interrupt bubble expansion and postpone the process wherein the bubbles merge into a large vapor mushroom and blanket the heated surface. The fin between the microchannels in the present study plays a role similar to the micro-post in the study performed by Jo et al. [29], and this delays the bubbles coalescence from two successive microchannels and is a potentially reasonable explanation for the increase in CHF. Furthermore, the wall superheat corresponding to CHF (ΔT_{CHF}) is also an important parameter in the application of electronic cooling with respect to the phase change [32]. The ΔT_{CHF} for BS, TS1, TS2, and TS3 are 20.5 °C, 10.5 °C, 5.6 °C, and 3.9 °C, respectively. Comprehensive comparisons of ΔT_{ONB}, $\mathrm{HTC}_{\max}$, CHF, and ΔT_{CHF} with respect to the different surfaces indicate that all the 3D heterogeneous wetting microchannel surfaces enhance boiling performance to a certain extent. However, different types of wettability combinations of the inner surface and fin top surface potentially do not satisfy the demand in which all the parameters of boiling should simultaneously achieve their optimum values. It is recommended that the optimal choice should be determined based on the goal of specific applications.

4.3. Bubble dynamics visualization

In order to further understand boiling mechanisms for the 3D heterogeneous wetting surface, bubble dynamics corresponding to the cases of ONB and $\mathrm{HTC}_{\max}$ are visualized with a high-speed camera. Fig. 10 shows the bubble patterns for ONB. With respect to the BS (Fig. 10a), nucleation bubbles are randomly distributed at the plain surface due to the sparse cavities as shown in Fig. 4a. Nucleation bubbles occur at both the inside of the microchannel and fin top surface of the TS1 (Fig. 10b) and TS3 (Fig. 10d), and more nucleation sites are observed on TS3 than those on TS1. Based on Eq. (7), increases in contact angle on the fin top surface leads to a wider range of active nucleation sites. It should be noted that bubble nucleation on TS2 (Fig. 10c) is observed to only occur at the inside of microchannel. This is because the superhydrophilic fin top surface requires more superheat than the hydrophobic inner surface to overcome the energy barrier of the phase change [21]. Furthermore, the sizes of the detached bubbles over the heated surface are observed to increase with increases in the ΔT_{ONB}, and this is potentially because increases in superheat lead to increases in the bubble growth rate.

Fig. 11 shows the bubble developing process for different surfaces corresponding to the cases of the maximum HTCs. The time interval between two successive pictures is 15 ms. With respect to BS with a slight hydrophilic property (Fig. 11a), the small bubble hills with liquid valleys in between are adhered to the heated surface (0 ms), and the bubble hills subsequently grow and aggregate in to a large bubble with a hollow well in the center (15 ms). It is inferred that the hollow well potentially provides a route for liquid rewetting to the heated surface. From 30 ms to 60 ms, the bubbles continue to increase with a higher growth rate in the horizontal direction as opposed to the vertical direction ($U_h > U_v$) and form an oblate shape bubble. The hollow well in the center of the oblate bubble disappears until the bubble detaches

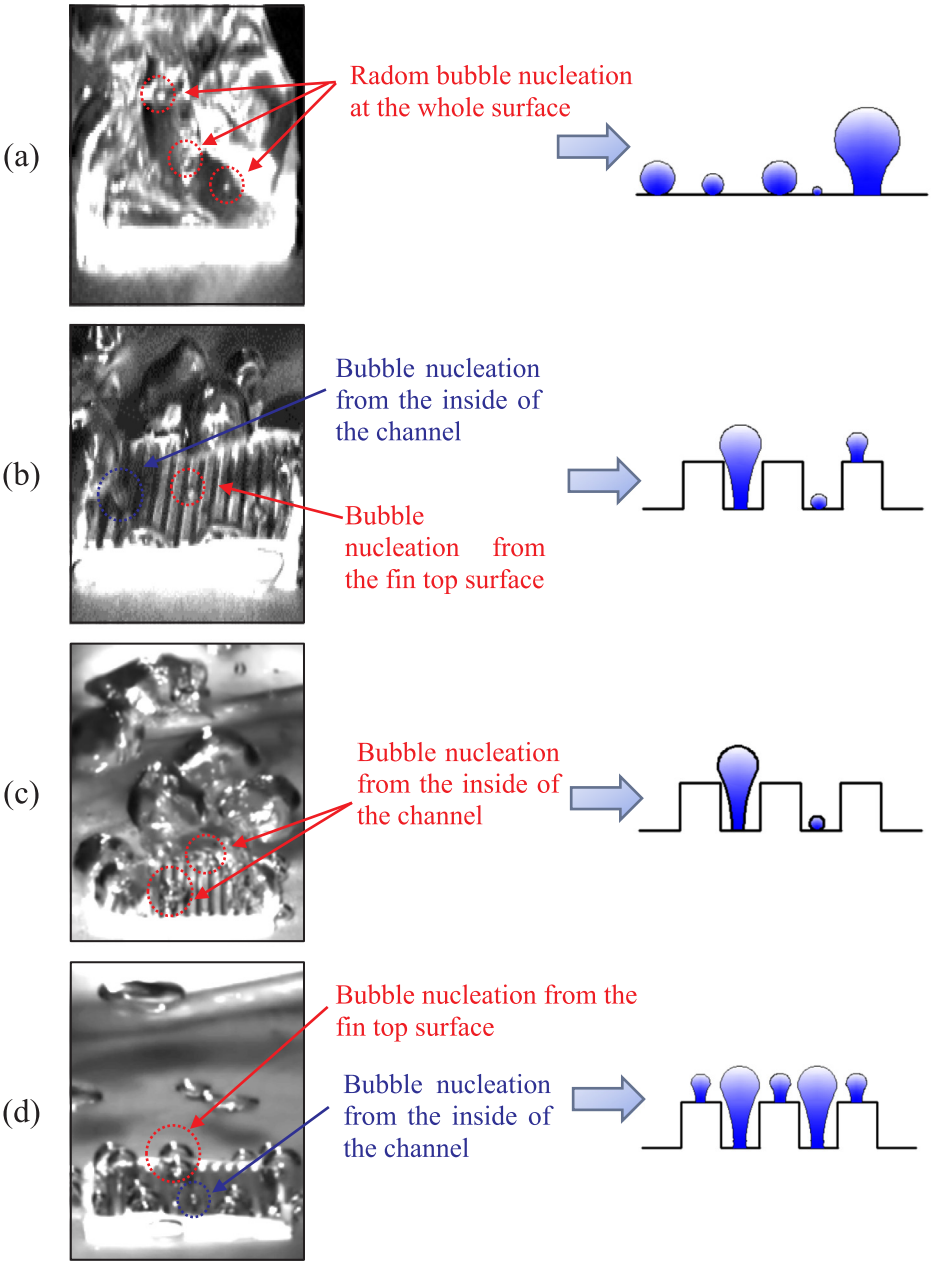

Fig. 10. Bubble dynamics for the onset of boiling. (a) BS, q = 272.0 kW/m^2; (b) TS1, q = 88.4 kW/m^2; (c) TS2, q = 133.6 kW/m^2; (d) TS3, q = 42.7 kW/m^2.

from the heated surface. Fig. 11b shows the bubble development on TS1 where the unsynchronized bubble growth forms several bubble hills with different sizes. Valleys continue to exist between the small bubble hills and large bubble hills and serve as liquid supply routes to the heated surface (0–30 ms). The valleys are closed when the small bubble hills are eaten by the large bubble hill (45–60 ms) and form a conical shape bubble ($U_h < U_v$). In this case, the liquid supply to the heated surface is only achieved through the gap between the conical bubble bottom and heated surface.

The bubbles left on the heated surface after the former bubble detachment are extremely small for TS2 (Fig. 11c). When the former bubble detaches, a thin vapor cloud exists and links the detaching bubble and heated surface (0 ms). Vapor jetting accompanied by bubble growth and aggregation is observed on the heated surface (15–30 ms), and makes the whole bubble appear similar to a swimming duck (45 ms). When the vapor jetting disappears, an oblate bubble with hollow well in the center is observed (60–75 ms). With respect to TS3 (Fig. 11d), the bubbles on the heated surface exhibit uniform sizes (0 ms) and their growth and coalescence appear synchronous and form four bubble hills with similar sizes (15–30 ms). It should be noted that the valley among the bubble hills appears to close (40 ms) and the bubble shape with four hills is maintained despite the continuous bubble growth.

The analysis of the bubble shape development on different surfaces identifies two new bubble growth patterns. The first type bubble growth pattern is termed as oblate bubble growth (OBG) in which the bubble growth rate in the horizontal direction exceeds that in the vertical direction. In this type of bubble growth pattern, liquid wells typically exist in the interior of the oblate bubble (Fig. 12a). The liquid supply to the heated surface proceeds through both the liquid wells and the gaps between the oblate bubble bottom and the heated surface. The second type bubble growth pattern is termed conical bubble growth (CBG) in which a conical shape bubble (Fig. 12b) or several conical bubbles (Fig. 11d) are formed due to a higher bubble growth rate in vertical than that in horizontal. The liquid supply is only accomplished by the gaps between the bubble bottom and the heated surface. The bubble

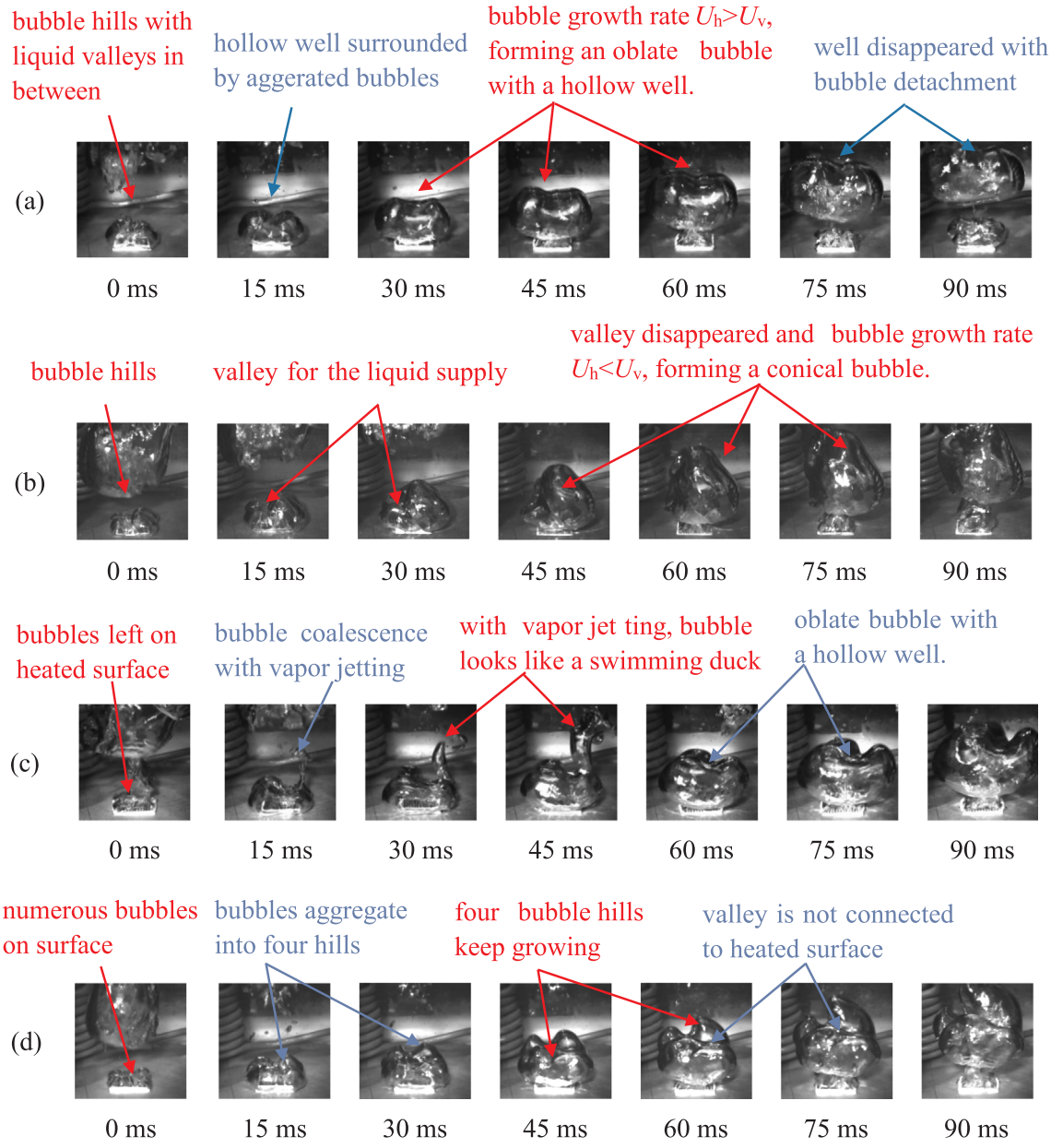

Fig. 11. Bubble dynamics corresponding to the cases of the maximum heat transfer coefficient for different surfaces. (a) BS, q = 980.4 kW/m^2; (b) TS1, q = 1617.8 kW/m^2; (c) TS2, q = 1549.8 kW/m^2; (d) TS3, q = 1295.1 kW/m^2.

shapes are either oblate or conical and are affected by the interactions of the leaving vapor and returning liquid near the heated surface. The forces applied on a vapor bubble include interfacial tension force, buoyancy force, and inertial force. The inertial effect is typically assumed to be neglected for the thermal bubble growth in a static liquid, and the bubble detaches from the heated surface when the buoyancy force exceeds the interfacial tension force. However, with respect to an enhanced boiling surface with a strong capillary liquid pumping ability, the inertial effect caused by the returning liquid is sufficiently high to affect the bubble growth pattern and bubble detachment. It is inferred that the oblate bubble growth pattern is caused by the inertial effect of the returning liquid, and this induces a squeezing effect on the growing bubble.

5. Conclusions

In the study, three types of 3D heterogeneous wetting microchannel surfaces were designed, fabricated, and characterized. Pool boiling experiments were conducted with the surfaces, and mechanisms for boiling heat transfer enhancement were discussed. From the test results and discussion, the following conclusions were drawn:

- 3D heterogeneous wetting microchannel surfaces (TS1, TS2, and TS3) with identical contact angles corresponding to 113.2° for the inner surface and contact angles of 88.6°, 8.6°, and 156.1°, respectively, for the fin top surfaces were fabricated via EDM and surface modification technologies. Multiscale pores and micro/nano compound microstructures were identified via SEM.
- The highest HTC for different 3D microchannel surfaces increased with increases in the contact angle of the fin top surface. The maximum HTC of 365.0 kW/m^2 K was obtained with TS3, which is 6.3 times that of BS. Furthermore, a higher contact angle of the fin top surface led to a lower ΔT_{ONB} and a smaller CHF. The lowest ΔT_{ONB} of 1.0 °C was obtained with TS3, and this was reduced by 8.6 °C when compared with that of the BS. The highest CHF of 162.7 W/cm^2 was achieved with TS2 with a superhydrophilic fin top

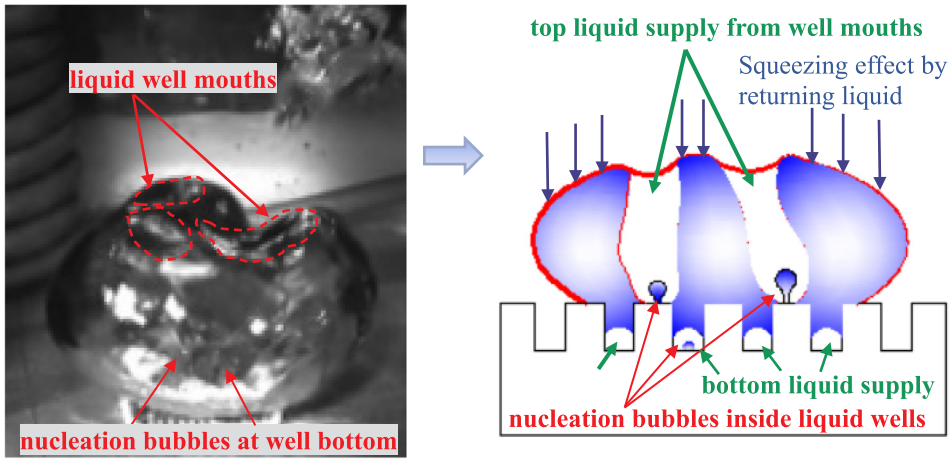

(a) Oblate bubble

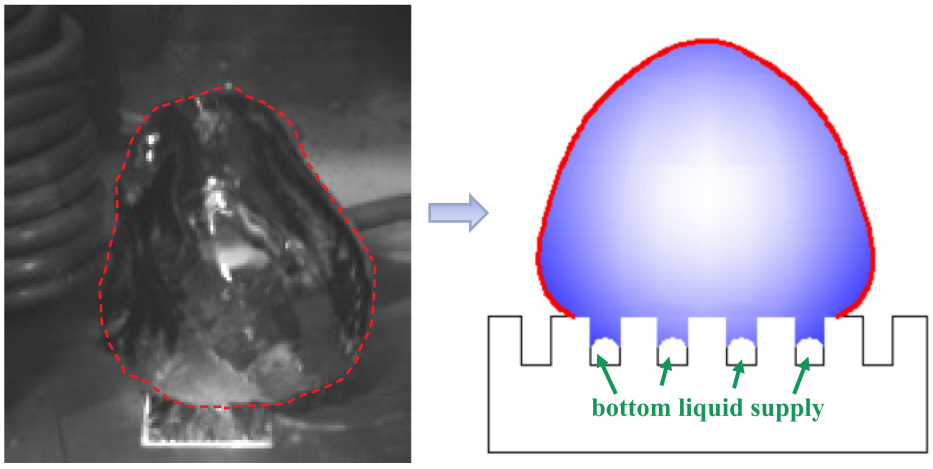

(b) Conical bubble

Fig. 12. Schematic of the two new bubble growth patterns.

surface and increased by 60% when compared with that of the BS.

- Synergistic effects of heterogeneous wettability and microstructures on boiling performance are summarized in terms of two aspects: (1) The multiscale pores and micro/nano compound structures provided numerous bubble nucleation sites while the hydrophobicity lowered the energy barrier for liquid/vapor phase change and increased the size range of active bubble nucleation sites. Thus, the ΔT_{ONB} decreased and HTC increased; (2) The microstructures provided a high capillary liquid pumping ability to draw the liquid back to the heated surface while the hydrophilicity strengthened the affinity of liquid with the heated surface. Thus, the CHF increased.
- Two new bubble growth patterns, namely “oblate bubble growth (OBG)” and “conical bubble growth (CBG)”, were identified via visualization. The bubble growth patterns were observed as closely related to the liquid supply route to the heated surface. The CBG appeared when the liquid supply was only achieved through the gaps between the growing bubble and heated surface. Conversely, the OBG occurred in the case where the liquid supply proceeded through both the liquid wells in the interior of the oblate bubble and gaps between the bubble and heated surface.
- The study provided original and deep insights into the synergistic effects of the wettability and microstructures on boiling heat transfer enhancement and acted as a guideline for the optimal design of novel boiling surfaces with excellent performance.

Acknowledgments

This work is support by the National Natural Science Foundation of China (51476057 and 51436004) and the Fundamental Research Funds for the Central Universities (2018MS014).

References

[1] V.P. Carey, Liquid-Vapor Phase-Change Phenomena, Hemisphere, Washington DC, 1992.
[2] J.R. Thome, Enhanced Boiling Heat Transfer, Hemisphere, New York, 1990.
[3] J. Kim, S. Jun, R. Laksnarain, S.M. You, Effect of surface roughness on pool boiling heat transfer at a heated surface having moderate wettability, Int. J. Heat Mass Trans. 101 (2016) 992–1002.
[4] B. Bourdon, E. Bertrand, P. DiMarco, M. Marengo, R. Rioboo, J. De Coninck, Wettability influence on the onset temperature of pool boiling: experimental evidence onto ultra-smooth surfaces, Adv. Colloid Interface Sci. 221 (2015) 34–40.
[5] G. Udaya Kumar, S. Suresh, M.R. Thansekhar, P. Dinesh Babu, Effect of diameter of metal nanowires on pool boiling heat transfer with FC-72, Appl. Surf. Sci. 423 (2017) 509–520.
[6] P.F. Xu, Q. Li, Y.M. Xuan, Enhanced boiling heat transfer on composite porous surface, Int. J. Heat Mass Trans. 80 (2015) 107–114.
[7] A.S. Moita, E. Teodori, A.L.N. Moreira, Influence of surface topography in the boiling mechanisms, Int. J. Heat Fluid 52 (2015) 50–63.
[8] S.G. Kandlikar, History, advances, and challenges in liquid flow and flow boiling

heat transfer in microchannels: a critical review, J. Heat Trans. 134 (3) (2012) 034001.
[9] Y.Y. Hsu, R.W. Graham, Transport Processes in Boiling and Two-Phase Systems, Hemisphere, Washington DC, 1976.
[10] Y. Takata, S. Hidaka, T. Uraguchi, Boiling feature on a super water-repellent surface, Heat Transfer Eng. 27 (2006) 25–30.
[11] H.J. Jo, H. Kim, H.S. Ahn, S. Kang, J. Kim, J.S. Shin, M.H. Kim, Experimental study of pool boiling for enhancing the boiling heat transfer by hydrophobic dots on silicon surface, Trans. Korean Soc. Mech. Eng. B 34 (2010) 655–663.
[12] B.S. Kim, G. Choi, D. Shim, K.M. Kim, H.H. Cho, Surface roughening for hemi-wicking and its impact on convective boiling heat transfer, Int. J. Heat Mass Trans. 102 (2016) 1100–1107.
[13] Y.F. Li, G.D. Xia, Y.T. Jia, Y. Cheng, J. Wang, Experimental investigation of flow boiling performance in microchannels with and without triangular cavities – a comparative study, Int. J. Heat Mass Trans. 108 (2017) 1511–1526.
[14] A. Jaikumar, S.G. Kandlikar, Enhanced pool boiling heat transfer mechanisms for selectively sintered open microchannels, Int. J. Heat Mass Trans. 88 (2015) 652–661.
[15] L.N. Dong, X.J. Quan, P. Cheng, An experimental investigation of enhanced pool boiling heat transfer from surfaces with micro/nano-structures, Int. J. Heat Mass Trans. 71 (2014) 189–196.
[16] H. Honda, J.J. Wei, Enhanced boiling heat transfer from electronic components by use of surface microstructures, Exp. Therm. Fluid Sci. 28 (2014) 159–169.
[17] K. Xin, Y.H. Zhang, J.J. Wei, Experimental study of pool boiling heat transfer on novel bistructured surfaces based on micro-pin-finned structure, Exp. Therm. Fluid Sci. 91 (2018) 9–19.
[18] K.H. Chu, R. Enright, E.N. Wang, Structured surfaces for enhanced pool boiling heat transfer, Appl. Phys. Lett. 100 (2012) 241603.
[19] H. O'Hanley, C. Coyle, J. Buongiorno, T. Mackerel, L.W. Hu, M. Rubner, B. Cohen, Separate effects of surface roughness, wettability, and porosity on the boiling critical heat flux, Appl. Phys. Lett. 103 (2013) 024102.
[20] H.S. Ahn, G.C. Lee, J. Kim, M.H. Kim, The effect of capillary wicking action of micro/nano structures on pool boiling critical heat flux, Int. J. Heat Mass Trans. 55 (2012) 89–92.
[21] S.H. Kim, G.C. Lee, J.Y. Kang, K. Moriyama, H.S. Park, M.H. Kim, The role of surface energy in heterogeneous bubble growth on ideal surface, Int. J. Heat Mass Trans. 108 (2017) 1901–1909.
[22] Y. Nam, J. Wu, G. Warrier, Y.S. Ju, Experimental and numerical study of single bubble dynamics on a hydrophobic surface, J. Heat Trans. 131 (2009) 121004.
[23] A.R. Betz, J. Xu, H.H. Qiu, D. Attinger, Does surfaces with mixed hydrophilic and hydrophobic areas enhance pool boiling? Appl. Phys. Lett. 97 (2010) 141909.
[24] A.R. Betz, J. Jenkins, C.J. Kim, D. Attinger, Boiling heat transfer on superhydrophilic, superhydrophobic, and superbiphilic surfaces, Int. J. Heat Mass Trans. 57 (2013) 733–741.
[25] H.J. Jo, S.H. Kim, H.S. Park, M.H. Kim, Critical heat flux and nucleate boiling on several heterogeneous wetting surfaces: controlled hydrophobic patterns on a hydrophilic substrate, Int. J. Multiphase Fl. 62 (2014) 101–109.
[26] H.B. He, K. Furusato, M. Yamada, B. Shen, S. Hidaka, M. Kohno, K. Takahashi, Y. Takata, Efficiency enhancement of a loop thermosyphon on a mixed-wettability evaporator surface, Appl. Therm. Eng. 123 (2017) 1245–1254.
[27] C.C. Hsu, M.R. Lee, C.H. Wu, P.H. Chen, Effect of interlaced wettability on horizontal copper cylinders in nucleate pool boiling, Appl. Therm. Eng. 112 (2017) 1187–1194.
[28] C. Sujith Kumar, Y.W. Chang, P.H. Chen, Effect of heterogeneous wettable structures on pool boiling performance of cylindrical copper surfaces, Appl. Therm. Eng. 127 (2017) 1184–1193.
[29] H.J. Jo, D.I. Yu, H. Noh, H.S. Park, M.H. Kim, Boiling on spatially controlled heterogeneous surfaces: Wettability patterns on microstructures, Appl. Phys. Lett. 106 (2015) 181602.
[30] H.W. Coleman, W.G. Steele, Experimentation and Uncertainty Analysis for Engineers, second ed., John Wiley & Sons Inc., 1999.
[31] X.B. Ji, J.L. Xu, Z.W. Zhao, W.L. Yang, Pool boiling heat transfer on uniform and non-uniform porous coating surfaces, Exp. Therm. Fluid Sci. 48 (2013) 198–212.
[32] I. Mudawar, Assessment of high-heat-flux thermal management schemes, IEEE T. Compon. Pack. 24 (2) (2011) 122–141.
[33] B. Shen, M. Yamada, S. Hidaka, J.W. Liu, J. Shiomi, G. Amberg, M.D. Quang, M. Kohno, K. Takahashi, Y. Takata, Early onset of nucleate boiling on gas-covered biphilic surfaces, Sci. Rep. 7 (2017) 2036.
[34] B.B. Mikic, W.M. Rohsenow, A new correlation of pool-boiling data including effect of heating surface characteristics, J. Heat Trans. 91 (1969) 245.
[35] Y.Y. Hsu, On the size range of active nucleation cavities on a heating surface, J. Heat Trans. 84 (1962) 207–213.
[36] N. Zuber, Hydrodynamic Aspects of Boiling Heat Transfer, Ph.D. Thesis, UCLA, 1959.
[37] M. Kaviany, Principles of Heat Transfer in Porous Media, Springer, New York, 1999.
[38] S.G. Liter, M. Kaviany, Pool-boiling CHF enhancement by modulated porous-layer coating: theory and experiment, Int. J. Heat Mass Trans. 44 (2001) 4287–4311.